Journal of the European Ceramic Society 43 (2023) 99–108

Contents lists available at ScienceDirect

Journal of the European Ceramic Society

journal homepage: www.elsevier.com/locate/jeurceramsoc

Low-temperature sintering and enhanced stability of fluorine-modified $BaZr_{0.8}Y_{0.2}O_{3-\delta}$ synthesised by a sol-gel alkoxide route

Ángel Triviño-Peláez, Jadra Mosa, Domingo Pérez-Coll, Mario Aparicio, Glenn C. Mather *

Instituto de Cerámica y Vidrio (CSIC), C/ Kelsen 5, Campus de Cantoblanco, 28049 Madrid, Spain

ARTICLE INFO

Keywords:
Proton-conducting perovskites
Barium zirconate
BZY
Sol-gel
Protonic ceramic cells

ABSTRACT

Sol-gel synthesis using alkoxides is employed to obtain fluorine-modified $BaZr_{0.8}Y_{0.2}O_{3-\delta}$ nanopowders with Ba excess at 750 °C. Possible effects of F loss at high temperature were limited on densifying at the low temperature of 1200 °C for 4 h on addition of ZnO as sintering agent. The presence of F in sintered samples was confirmed by X-ray photoelectron spectroscopy (XPS) and time-of-flight secondary ion mass spectrometry. XPS and Raman spectroscopy indicated that F doping of BZY inhibits carbonate formation. Conductivity measurements for prolonged periods in wet H_2-containing and CO_2-containing atmospheres at 500 °C also demonstrated chemical stability. The temperature dependence of the electrical conductivity of sintered samples in wet and dry N_2 and O_2 indicates that the grain-boundary dominates the electrical behaviour to 500 °C, above which the bulk process dominates. Ionic conduction is prevalent at low temperature, with a transition to a mixed ionic-electronic conducting behaviour at 450 °C.

1. Introduction

Yttrium-doped barium zirconate perovskites ($BaZr(Y)O_{3-\delta}$, BZY) are excellent candidates for application in protonic ceramic fuel cells (PCFCs) and protonic ceramic electrolyser cells (PCECs) due to good protonic conductivity in an intermediate temperature range (400–700 °C) and improved stability against acidic gases such as CO_2 compared to the barium cerate-based analogues [1–3]. The mixed protonic-electronic conductivity of BZY-metal composite membranes may also be exploited for hydrogen-separation [4,5]. Membrane reactors based on BZY that promote (de)hydrogenation reactions are also of considerable interest, with co-ionic conduction of oxide ions and protons facilitating, for example, nonoxidative methane dehydroaromatization [6].

The high sintering temperatures which are usually required to overcome the refractory nature of BZY and densify membranes cause barium loss and elemental segregation. Alternative synthesis routes have been employed with $Ba(Ce,Zr)O_3$-based solid solutions to improve sinterability and exploit the higher ionic conductivity offered by higher Ce content on the Zr site of the perovskite [7,8]. Nevertheless, BZY compositions remain of interest due to their higher stability and several strategies have been successful in lowering the sintering temperature, including the employment of dopants [9] and sintering agents [10–13], as well as reactive sintering [14,15]. One of the more studied sintering additives is ZnO, as it offers a low sintering temperature (1300 °C) and is not known to form secondary phases [10,11,16]. Recently, it was shown that the mechanism of ZnO addition (substituting for Y, Zr or as B-site cation excess) does not significantly alter the degree of densification but minor differences in the electrical properties were observed [17].

We recently reported that the sintering temperature for achieving dense BZY membranes could be lowered to 1200 °C on synthesising reactive powder by a sol-gel method, and employing both ZnO as sintering aid and Ba excess in the starting composition [18]. This very low sintering temperature facilitates co-sintering with adjacent cell components and limits BaO loss which occurs above 1250 °C. It was found that a higher specific grain-boundary conductivity for the BZY sintered at low temperature largely compensated a slightly lower bulk conductivity compared to the same composition sintered at higher temperature.

Recently, Gao et al. [19] showed that F doping on the anion sublattice of BZY improved proton conductivity, suggesting that weaker cation-oxygen bonds enhanced the mobility of ionic-transport species. Similarly, Tarasova et al. [20] reported that Cl- and F-doping of the double perovskite $Ba_2CaNbO_{6-\delta}$ increases oxide-ion and proton mobilities. We also recently found enhanced oxide-ion and proton conductivity in Br-synthesised $BaCe_{0.9}Y_{0.2}O_{3-\delta}$ in wet and dry conditions, respectively [21]. However, high-temperature sintering led to almost complete evaporation of Br and the improved conductivity was

* Corresponding author.
E-mail address: mather@icv.csic.es (G.C. Mather).

https://doi.org/10.1016/j.jeurceramsoc.2022.09.042
Received 7 April 2022; Received in revised form 10 August 2022; Accepted 22 September 2022
Available online 23 September 2022

attributed to a greater vacancy concentration arising from Ba deficiency [21,22]. In contrast, a study of Zhou et al.[23] reported impaired conductivity of $BaCe_{0.9}Gd_{0.1}O_{3-\delta}$ in air on doping with F or Cl.

It is well documented that the basic nature of perovskite proton conductors may give rise to stability problems, particularly in acidic gases, and more so for the cerate series than for the zirconates [2]. However, the stability of barium zirconate in high water-vapour partial pressures is poor [24], and carbonate species form on the surface of BZY in CO_2-containing atmospheres, which may inhibit surface reactions [25,26]. In addition to altering electrical properties, halogen doping may be expected to improve stability. Whereas F atoms are more electronegative than elemental O and may thus lower the basicity of the anion sublattice, Cl and Br are less electronegative (more basic) but the lower charge of the monovalent halogen anions may impart less basic character than O^{2-} anions, thereby improving stability in acidic environments. Wang et al. [27] reported improved stability and higher proton conductivity in Cl-doped $BaCe_{0.8}Sm_{0.2}O_{3-\delta}$, whereas we found that Br-synthesised $BaCe_{0.9}Y_{0.2}O_{3-\delta}$, but with no Br in the final composition, exhibited lower stability in CO_2 than the parent phase without Br addition [21].

Reports on the effects of halogen doping both on stability and electrical properties are, thus, somewhat contradictory. The behaviour may be complex to interpret, partly due to high-temperature sintering of ceramic membranes, which may promote halogen evaporation leading to uncontrolled amounts of halogen in the final sintered body. Moreover, electrical properties detailing contributions of different transport species usually require specific methods [28,29].

Here, we report the synthesis of F-doped $BaZr_{0.8}Y_{0.2}O_{3-\delta}$ by sol-gel, employing an alkoxide route to introduce fluorine and achieve highly sinterable nanopowders at low temperature. The presence of F in the final sintered body is examined by X-ray photoelectronic spectroscopy (XPS) and time-of-flight secondary ion mass spectrometry (ToF-SIMS). A comparison of chemical stability of F-doped and F-free samples is undertaken employing Raman spectroscopy and XPS, in addition to prolonged conductivity measurements in wet CO_2- and H_2-containing atmospheres. Detailed electrical measurements are also performed in wet and dry oxygen and nitrogen to determine the effects of F doping and sintering temperature on the electrical-transport properties.

2. Experimental

Nominal compositions of the series $BaZr_{0.8}Y_{0.2}O_{3-\delta}F_x$, (x = 0 and 0.1, labelled hereafter as BZY20 and BZY20–10F, respectively) were prepared by a sol-gel processing route using alkoxide precursors. The synthesis procedure has been described previously [18,30], and shall only be summarised briefly. In the case of the F-doped material, BZY20–10F, trifluoroacetic acid was employed and the molar ratios of barium: yttrium (III) butoxide: zirconium (IV) propoxide: trifluoroacetic acid: 2-methoxyethanol: water were 1.1:0.2:0.8:1/30:60:3; 10 mol% of barium excess was employed to achieve low-temperature densification and to limit the effects of barium loss during sintering [18]. Barium filings were dissolved in excess 2-methoxyethanol while stirring at room temperature under an Ar atmosphere for 3 h to form a precipitate-free solution of barium alkoxide ($Ba(O_2C_3H_7)_2$). A solution of M-O-R (M: Ba, Y, Zr) species was obtained on addition of zirconium (IV) propoxide and yttrium (III) butoxide followed by controlled condensation reactions involving ionic exchange and formation of *n*-butanol and *i*-propanol. In the case of BZY20–10F, trifluoroacetic acid was added to the homogeneous mix of M-O-R species to provide the nominal content of fluorine, which is incorporated in the structure through reaction of trifluoroacetate anion with metal alkoxides. After stirring the solutions for 30 min at room temperature, a second solution of 2-methoxyethanol and water was then added dropwise to initiate hydrolysis and condensation reactions.

Homogeneous, transparent solutions were obtained after mixing for 3 h at room temperature. The organic solvent was largely removed in a rotavapor by vacuum distillation, yielding a very viscous caramel-like gel which was heated at 350 then 750 °C for 4 h under argon atmosphere to ensure the complete elimination of synthesis alcohols and water, with an intermediate step of grinding the product in an agate mortar.

$Zn(NO_3)_2{\cdot}6H_2O$ (Alfa Aesar, 99.998 %) as sintering aid was added to the powders (4 mol%) and the mixture ground in a Pulverisette 6 planetary ball mill for 2 h at 600 rpm in a medium of 2-propanol then sieved (100 μm). The powders were uniaxially pressed into pellets at 37.5 MPa then isostatically pressed to ~196–294 MPa (~2000–3000 kg/cm^2). Final firing of the pressed pellets was performed at 1200 °C for 4 h in air. Apparent density was determined from the geometric dimensions and mass of the sample.

X-ray diffraction (XRD) was employed to determine the progress of the sol-gel reaction using a Bruker D8 high-resolution diffractometer (monochromatic Cu Kα_1 radiation, $\lambda = 1.5406$ Å) over the range $20 \leq 2\theta \leq 100^o$. For preparation of fine powders for Rietveld refinement, the surface layer of sintered pellets was firstly polished off with SiC paper before grinding. Crystallite size, ϕ, was calculated from the X-ray diffraction powder profiles with the Scherrer formula:

$$\phi = \frac{0.94{\cdot}\lambda}{\cos(\theta){\cdot}\sqrt{B^2 - B_i^2}} \quad (1)$$

where θ corresponds to the angle of the most intense diffraction peak of the perovskite phase, B is the full width at half maximum, and B_i is the instrumental broadening; the constant value of 0.94 is a common factor used for spherical crystals [31]. A perovskite structural model was fitted to the XRD data by Rietveld refinement with the Fullprof software [32], employing a pseudo-Voigt profile function and refinement of selected background points.

A Hitachi S-4700 field-emission scanning electron microscope was used to observe the microstructures of fracture surfaces. The average grain size was determined from the micrographs by the linear-interception method employing the ImageJ software.

Raman spectroscopy was performed using a Confocal Micro-Raman instrument (Witec alpha-300R, Ulm, Germany) with laser excitation of 532 nm and a 100 × objective lens (NA = 0.9) for pellets heat-treated at 1200 °C for 4 h in air. The optical resolution diffraction of the confocal microscope is limited to 200 nm laterally and 500 nm vertically, and Raman spectral resolution of the system is down to 0.02 cm^{-1}. Surface chemical states of BZY20 and BZY20–10F pellets heat-treated at 1200 °C for 4 h were also studied by XPS using an Ar^+ ion source. X-ray photoelectron spectroscopy (XPS) data were acquired on a K-Alpha–Thermo Scientific spectrometer with a monochromatic Al Kα X-ray source (1486.68 eV). Elemental quantification was performed using the Shirley method for complete spectra and a peak fit program (Advantage 4.6 Thermo). Compositional depth profiling of the pellet BZY20-10F treated at 1200 °C for 4 h in air was carried out using a ToF-SIMS Ion Tof. A pulsed 25 kV Bi_3^{2+} ion source was employed for analysis over a 10 × 10 μm^2 area. Sputtering was performed using a 2 kV oxygen beam over a 250 × 250 mm^2 area. Data acquisition and post-processing analyses were carried out using Ion-Spec software.

Electrical behaviour was characterised by impedance spectroscopy employing an Autolab Frequency Response Analyser PGStat302N-FRA2 operating in the frequency range $0.1 \leq f \leq 10^6$ Hz using a signal amplitude of 50 mV. Pt paste (Metalor) was first painted on polished pellet surfaces, followed by firing at 950 °C for 1 h to prepare electrodes for measurement of the pellets. The temperature dependence of conductivity was determined in the temperature range 150–950 °C on cooling in steps of 50 °C in wet and dry flows of O_2 and N_2 regulated by Bronkhorst electronic mass-flow controllers; equilibration time at each temperature was at least 45 min (higher temperatures) and up to 1 h 30 min for lower temperatures. The gases were either passed through a drying column with a packed bed of commercial aluminosilicate and zeolite beads (Supelco) to achieve dry atmospheres, or were bubbled

through KBr-saturated H_2O at room temperature to obtain wet atmospheres ($pH_2O \sim 0.022$ atm). The impedance contributions were identified as bulk, grain-boundary and electrode processes from the capacitance values [33] and appropriate equivalent circuits were analysed with the Zview 2.9c program (Scribner Associates).

In addition to spectroscopic methods, stability was further assessed on monitoring the impedance response in wet ($pH_2O \sim 0.022$ atm) atmospheres of 90 % Ar-10 % CO_2 and 90 % N_2-10 % H_2 at 500 °C for periods up to 72 h followed by post-operation analysis by XRD. As carbonation of BZY-based ceramics is favoured at low temperatures, the chemical and mechanical stability was also evaluated on exposing fracture surfaces of dense pellets to laboratory air for up to 14 days followed by analysis by XRD of the milled samples.

3. Results and discussion

3.1. Phase analysis, crystal structure, densification and microstructure

Formation of perovskite material isostructural with $BaZrO_3$ (ICDD 6–0399) was confirmed by XRD for the nominal composition $BaZr_{0.8}Y_{0.2}O_{2.9-\delta}F_{0.1}$ on thermal treatment of the sol-gel powder at the low temperature of 750 °C under an Ar atmosphere. Rietveld refinement of the cubic perovskite structural model was performed (space group, $Pm\bar{3}m$), and is shown in Fig. 1 a); corresponding structural parameters and agreement factors are provided in Table 1.

A minor amount of $BaCO_3$ (ICDD 45–1471) was discerned, 3.21 wt%, as calculated by the refinement, indicating incomplete formation of the perovskite phase, most likely due to remaining organic compounds from the high content of alcohol of the precursors reacting with the initial excess of barium. The lattice parameter of BZY20–10F prepared at

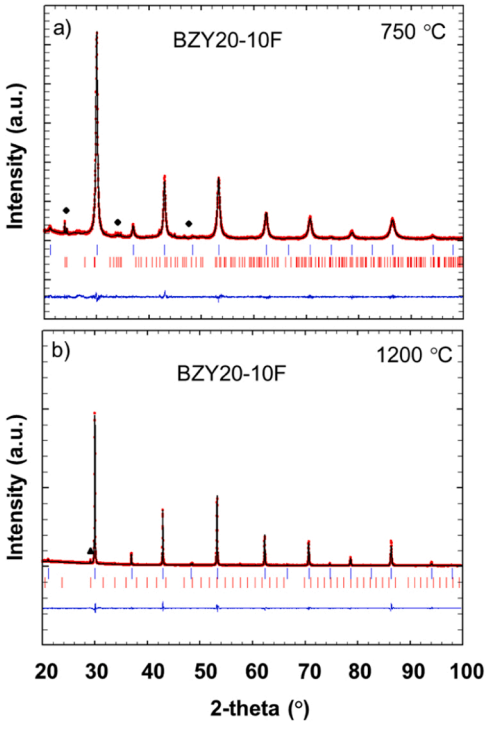

Fig. 1. XRD Rietveld refinement plots of BZY20-10F showing observed (red circles), calculated (continuous black line) and difference (continuous blue line at bottom) diffraction profiles a) powder heat treated at 750 °C for 4 h under an Ar atmosphere showing $BaCO_3$ peaks as diamonds (space group *Pmcn*); b) sample sintered at 1200 °C for 4 h showing Y_2O_3 peaks as triangles (space group, $Ia\bar{3}$). Top and bottom vertical bars indicate the expected position of Bragg peaks of the simple cubic perovskite phase (space group, $Pm\bar{3}m$) and second phase, respectively.

Table 1
Structural parameters and agreement factors for BZY20–10F, prepared by sol gel with Ba excess and addition of ZnO sintering aid, heat treated at 750 °C then 1200 °C, obtained from XRD data.

	750 °C ($Pm\bar{3}m$)	1200 °C ($Pm\bar{3}m$)
a (Å)*	4.2080(1)	4.21051(3)
V(Å^3)*	74.514(3)	74.647(1)
Ba position	½ ½ ½	½ ½ ½
$U_{iso}\times$ 100 (Å^2)	1.36(5)	0.90(3)
Occ	1.0	1.0
Zr/Y position	0 0 0	0 0 0
$U_{iso}\times$ 100 (Å^2)	0.98(6)	0.56(4)
Occ	0.8/0.2	0.8/0.2
O/F position	½ 0 0	½ 0 0
$U_{iso}\times$ 100 (Å^2)	1.2(1)	0.6(1)
Occ	2.85/0.1	2.85/0.1
χ^2	1.17	2.00
R_{exp}	7.35	5.69
R_{wp}	7.95	8.05
$R_{B,BZY}$	1.30	4.06

* cell parameter and volume were determined with internal CaF_2 standard then fixed during Rietveld refinement

750 °C, a = 4.2080(1) Å, is lower than expected for fully reacted BZY20. However, it is known that the lattice parameter of BZY20 goes through a maximum at 1250 °C, with lower lattice parameter below this temperature attributable to incomplete Ba incorporation in the structure [34]. The average crystallite size of BZY20–10F on heat treatment at 750 °C, calculated from the (110) XRD peak by the Debye-Scherrer equation, was 25 nm, in the same range but slightly lower than that reported for F-free BZY20 prepared in the same manner [18]. A scanning electron micrograph of the sol-gel powder treated at 750 °C, Fig. 2a), shows agglomerated crystallites and confirms the nanometric grain size.

Ceramic bodies with relative density (r.d.) ~ 95 % were obtained for F-containing BZY on addition of 4 mol% ZnO as sintering aid to the sol-gel powder followed by isostatic pressing then sintering at 1200 °C for 4 h. As noted in our previous work [18], preparation of the sol-gel material with the nominally stoichiometric amount of Ba led to much lower densities on sintering at the same temperature, ~ 83 % r.d, so these compositions were excluded from further study. A scanning electron micrograph of a fracture surface of the material sintered at 1200 °C for 4 h is shown in Fig. 2b); grain size was calculated to be ca. 228 nm for the sintered BZY20-10F. The XRD powder data of BZY20-10F sintered at 1200 °C were employed for Rietveld refinement of the cubic perovskite structural model ($Pm\bar{3}m$ space group, Fig. 1b)). The lattice parameter of the BZY-based phases was first determined on refining the structure with the addition of CaF_2 as internal lattice-parameter standard (lattice parameters under different heat treatments and comparison with BZY20 lattice parameters are shown in Fig. S1). The observed XRD profile of BZY20–10F sintered at 1200 °C and the difference between observed and calculated patterns are shown in Fig. 2b); selected structural parameters and agreement factors for the two phases are shown in Table 1. Vestiges of Y_2O_3 (~ 3 wt%; ICDD 41–1105) were discerned in the XRD patterns of samples treated at 1200 °C. However, as was the case for the F-free analogue BZY20 [18], material sintered at 1650 °C was free of Y_2O_3 indicating that its presence at the lower temperature may be the result of kinetic factors (the XRD powder pattern and Rietveld refinement plot of BZY20–10F sintered at 1650 °C are shown in Fig. S2). It was previously argued that, since some $BaCO_3$ is present at the lower temperature of 750 °C, but not Y_2O_3, then a minor amount of Y is likely to reside on the A-site of the perovskite at this temperature [18]. Ba then displaces the A-site yttrium at 1200 °C, forming Y_2O_3 as a second phase. At still high sintering temperatures, further incorporation of Ba on the A site occurs concomitantly with incorporation of Y from Y_2O_3 on the B site. The lattice parameter, and corresponding lattice volume, is slightly higher for the F-synthesised material sintered at 1200 °C (a = 4.21055(3) Å in comparison to 4.20521(4) Å for BZY20) contrary to the

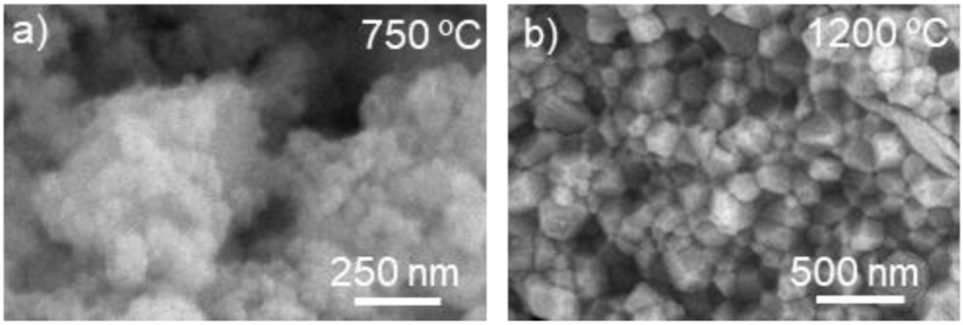

Fig. 2. SEM images of a) sol gel powder of BZY20-10F heat treated at 750 °C; b) fresh fracture surface of dense pellet of BZY20-10F sintered at 1200 °C for 4 h with Ba excess and ZnO sintering aid.

expectation that substitution of the larger O^{2-} anion for the smaller F^- anion [35] will lower lattice parameter; the shift in lattice parameter is illustrated in Fig. S3 from the (1 1 0) peak of the XRD patterns.

In the parent BZY20 material, the creation of oxygen vacancies is given by the following defect reaction (Kröger-Vink notation):

$$BaO + 0.8ZrO_2 + 0.1Y_2O_3 \leftrightarrow Ba_{Ba}^{x} + 0.8Zr_{Zr}^{x} + 0.2Y_{Zr}^{'} + 2.9O_{O}^{x} + 0.1V_{O}^{\cdot\cdot} \quad (2)$$

However, in the case of the flourine-doped BZY20-10F sample, the concentration of nominal oxygen vacancies is expected to be lower:

$$0.95BaO + 0.8ZrO_2 + 0.1Y_2O_3 + 0.05BaF_2 \leftrightarrow Ba_{Ba}^{x} + 0.8Zr_{Zr}^{x} + 0.2Y_{Zr}^{'} + 2.85O_{O}^{x} + 0.1F_{O}^{\cdot} + 0.05V_{O}^{\cdot\cdot} \quad (3)$$

Computer simulations indicate that, in the absence of changes in oxidation state of the cations, the formation of an oxygen vacancy produces a contracting effect on the lattice [36]. Although the higher lattice parameter for the F-doped phase may result, therefore, from the lower nominal oxide-ion vacancy concentration, a more significant contributing factor to the larger lattice parameter of BZY20–10F at 1200 °C in comparison to the F-free analogue may be that the Ba content of the former is slightly greater at this sintering temperature. As mentioned, the lattice parameter of BZY20 increases to 1250 °C with increasing Ba incorporation [34]. It is possible that the reaction kinetics are faster, with greater incorporation of Ba in BZY20-10F at 1200 °C than in the F-free analogue, leading to a slightly greater lattice parameter for the F-containing phase. Although $BaCO_3$ is not observed by XRD at 1200 °C in either phase, the lattice parameter of BZY20 prepared with Ba excess and ZnO sintering agent sintered at 1650 °C increases with respect to that at 1200 °C, further suggesting some Ba is still present in an amorphous state at 1200 °C in BZY20 (Fig. S1). In contrast, the lattice parameter of BZY20-10F is slightly lower at 1650 °C than at 1200 °C, indicating that Ba incorporation is greater at 1200 °C, and that thereafter some Ba evaporation takes place between these temperatures [18]. We note that, at 1650 °C, the lattice parameter of BZY20–10F is actually slightly lower than that of BZY20, as may be expected on consideration of the ionic radii of the halogen dopant (Fig. S1); this may have a much larger effect on the lattice parameter than the lower vacancy content arising from F doping (Eq.(3)). However, since evaporation of F may occur quite readily at 1650 °C, this sample was not subject to further study.

3.2. Spectroscopic analysis of stability and fluorine content

One of the principal drawbacks of proton-conducting perovskites is that the alkaline-earth A-site cation tends to form carbonate initiating at the surface in CO_2-containing atmospheres, particularly at low temperature [22,25]. As mentioned in the introduction, halogen dopants may improve stability but their exact role and degree of incorporation may lead to inconsistent results due to the tendency for the halogens to evaporate on high-temperature sintering. To confirm the incorporation of fluorine and its effect on stability in the nominal composition $BaZr_{0.8}Y_{0.2}O_{3-\delta}F_{0.1}$, prepared and densified by the low-temperature route used in the present study, the spectroscopic structural techniques Raman Spectroscopy, X-ray Photoemission Spectroscopy and Time-of-Flight Secondary Ion Mass Spectrometry, involving surface or bulk analysis of the material in the form of powder or sintered body, were employed.

3.2.1. Raman spectroscopy

Raman spectroscopy of BZY20 and BZY20–10F (Fig. 3a)) is consistent with cubic perovskite (space group $Pm\bar{3}m$), which forms at 750 °C, in accordance with the XRD analysis. Raman scattering corresponding to asymmetric modes of the BO_6 octahedra are found at 107, 180, 458 and 732 cm^{-1} for first order A1(TO) modes, and at 231 and 408 cm^{-1} for second-order modes. The modes located at 500 cm^{-1} and the broad region 600 – 800 cm^{-1} are assigned to A1(LO)/E(LO) and A1(TO) vibrations of locally distorted $Zr(Y)O_6$ octahedra [37–39]. The presence of $BaCO_3$ is confirmed from the active modes at 132, 150, 451, 691, 834, 1000 and 1060 cm^{-1}, attributable to carbonate-stretching vibrations [40], in accordance with the XRD data. However, the $BaCO_3$ bands are no longer observed for the BZY20–10F sample sintered at 1200 °C, (Fig. 3b)). It should be noted that the intensities of the $BaCO_3$ bands in the sample BZY20–10F heat-treated at 750 °C are relatively high in comparison to those of the pervoskite, as $BaCO_3$, with space group *Pmcn*, is more sensitive to Raman spectroscopy [39]. The Raman spectra of the perovskite bands of samples with and without F-doping are, in general, similar, with the exception of the band at 720 cm^{-1}, which undergoes a moderate displacement to high energy (5 cm^{-1}), a change in the band morphology, and the appearance of a shoulder at 705 cm^{-1} in the F-containing sample for BZY20–10F heat-treated at both 750 and 1200 °C.

Such modifications have been assigned to symmetry effects on incorporating B-site elements and consumption of oxygen vacancies [41–43]. Other authors have attributed this blue shift of the band at 720 cm^{-1}, which occurs in F-doped BZY, to a volume expansion, which would concur with the lattice-parameter data determined by XRD (Fig. S1) [44,45]. Although there is no additional Raman band related to halogen vibrational modes, modification of the band at 720 cm^{-1} suggests the possible incorporation of fluorine in the perovskite [46,47].

3.2.2. X-ray Photoemission Spectroscopy (XPS)

XPS was employed to evaluate homogeneity, carbonate formation and the presence of fluorine in ceramic pellets of BZY20 and BZY20-10F sintered at 1200 °C. Fig. 4 a) indicates the modifications undergone by the atomic orbitals $Zn(2p_{3/2})$, Zr(3p), $Ba(3d_{5/2})$, Y(3d), Zr (3d)+Ba(4p), and O(1 s) for the BZY20 sample, and additionally the F(1 s) orbital for BZY20–10F. The two spectra are similar, apart from the presence of the peak attributable to F(1 s) at 685.7 eV in the BZY20-10F spectrum [48–50]. There are no observable variations between the spectra for the

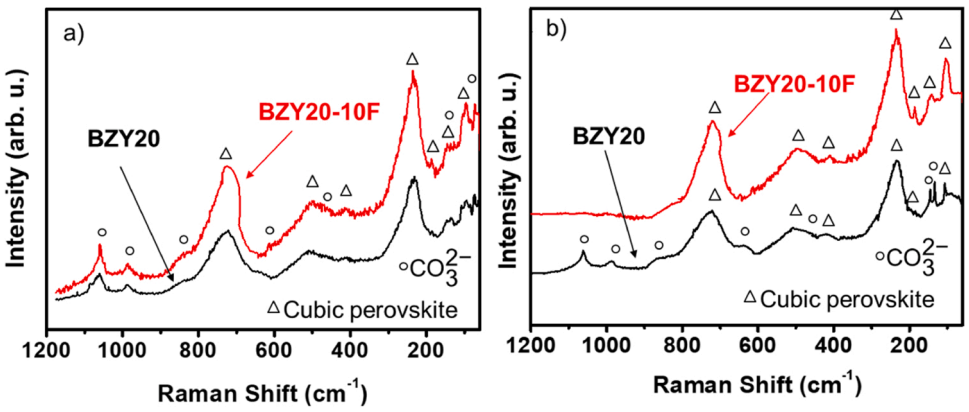

Fig. 3. Raman spectra of BZY20 (black) and BZY20-10F (red) powders calcined at a) 750 °C for 4 h and b) 1200 °C for 4 h.

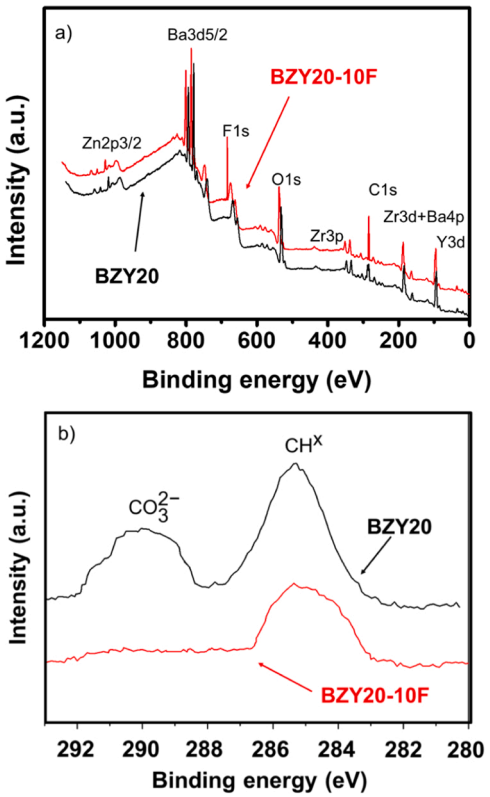

Fig. 4. a) XPS profile of BZY20 and BZY20-10F sintered at 1200 °C; b) C 1 s peaks for BZY20 and BZY20-10F pellets.

Zn, Zr, Y or Ba peaks. Principal bands associated with Zn ($2p_{3/2}$) and Ba ($3d_{5/2}$) are centred at 1028 and 785.2 eV, respectively, whereas the signals at 352.9 and 337.5 eV may be related to Zr(3p). Signals from the Zr3d+Ba4p and Y(3d) orbitals appear at 190–180 and 164 eV, respectively. Fig. 4b) shows the X-ray photoelectron spectra in the energy zone of the C(1 s) bond for BZY20 and BZY20–10F pellets heat-treated at 1200 °C in air. The C(1s) singlet was split into a doublet for BZY20, implying two distinguishable oxide species at 284.7 and 289.8 eV related to the presence of hydrocarbon (CH_x species) and carbonate formation, respectively [41,51,52]. The peak at 289.8 eV associated with carbonate species is of much less intensity in the case of the F-containing sample. Hydrocarbon species are a common impurity which form at the surface of the sample during measurement in UHV systems, and are often used as an internal standard to reference other elements [53]. It is expected that XPS detects surface carbonate due to the thermal treatment of the surfaces in air. Although it was previously shown that BZY20 prepared by the route employed in this study is stable for prolonged periods in wet and dry CO_2- and H_2-containing atmospheres [18], the presence of F may further improve stability towards carbonation on lowering the basicity of the anion sublattice. The presence of carbonate phase ($BaCO_3$) at the surface in F-free BZY20 and its near absence in BZY20–10F is consistent with the Raman spectroscopy results.

3.2.3. *Time-of-flight secondary ion mass spectrometry*

The principal ions present in BZY20–10F ceramic bodies densified at 1200 °C were examined by ToF-SIMS, providing an elemental distribution with depth from the surface for the bulk material (Fig. 5). The compositional profile reveals a homogeneous distribution of the elements as a function of depth up to and including the interface with the silicon sample holder (~ 300 s of bombardment). As in the case of the XPS analysis, the presence of F^- anions is apparent at the surface, with the depth profile indicating their location throughout the measured sample depth. Nevertheless, the surface is richer in F^- than the bulk of the sample with its concentration diminishing steadily as a function of depth. The homogeneous distribution of the other ions present in the perovskite structure BaO^-, YO^- and ZrO^- are also shown, in addition to ZnO^-; previous results indicate that Zn is to be expected both in the perovskite lattice and in the grain boundaries [17].

3.3. *Evaluation of stability with conductivity measurements*

Our previous study indicated that the Ba excess employed in the starting composition to promote low-temperature densification did not contribute to deteriorating stability. Hence, it is also unlikely that BaO is present in the grain boundaries at the sintering temperature of 1200 °C. In a stability assessment of the fluorine-doped zirconate under potentially reactive atmospheres, conductivity measurements in wet

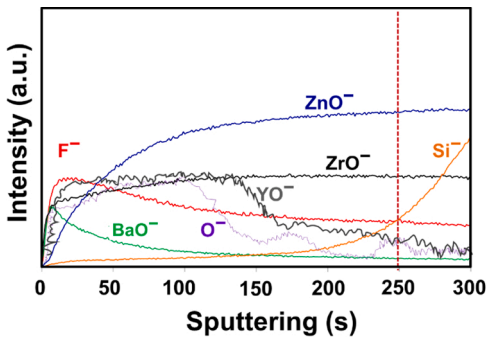

Fig. 5. ToF-SIMS depth profile of BZY20–10F pellet sintered at 1200 °C.

atmospheres of 90 %Ar-10 %CO_2 and 90 %N_2-10 %H_2 were performed for prolonged periods. Fig. 6a) shows that, after a period of ~ 24 h stabilisation, the total conductivity of BZY20-10F is essentially constant at 500 °C in the CO_2-containing atmosphere. The conductivity recorded in wet 90 %N_2-10 %H_2 at 500 °C, after an initial period of stabilisation of 4 h, provides a similar stable profile after ~ 3 days. Slight oscillations in conductivity were observed in both atmospheres and were attributed to small changes in the room temperature of the bubbler system during the ageing periods. Mechanical integrity of the sample was completely retained after the ageing exposure in both atmospheres, without any indication of degradation. Moreover, XRD powder patterns of the milled pellet subsequent to the exposure indicated an absence of carbonation or hydroxide products, Fig. 6b).

The stability was evaluated further by exposing pellet fragments (r.d. in the range 94–99 %) to laboratory air for 14 days. Carbonation may be favoured at low temperature, and it is known, for example, that degradation of $BaCeO_3$-based compositions occurs under such conditions [22]. In the case BZY20-10F, neither carbonate formation nor mechanical breakdown was observed visually after the exposure period (inset of Fig. 6c)). A similar behaviour was previously observed for BZY20 [18]. The XRD powder patterns of the ceramic pieces subsequent to exposure in air were free of barium carbonate or hydroxide (Fig. 6c)) Hence, as was the case in our earlier study [18], the Ba superstoichiometry present in the reactant mixture is unlikely to be present as BaO in the final sintered body. Nevertheless, although both BZY20 and BZY20-10F are stable under the measured conditions, the greater carbonation of BZY20 determined by spectroscopic methods likely indicates that the long-term stability of the F-containing material is greater.

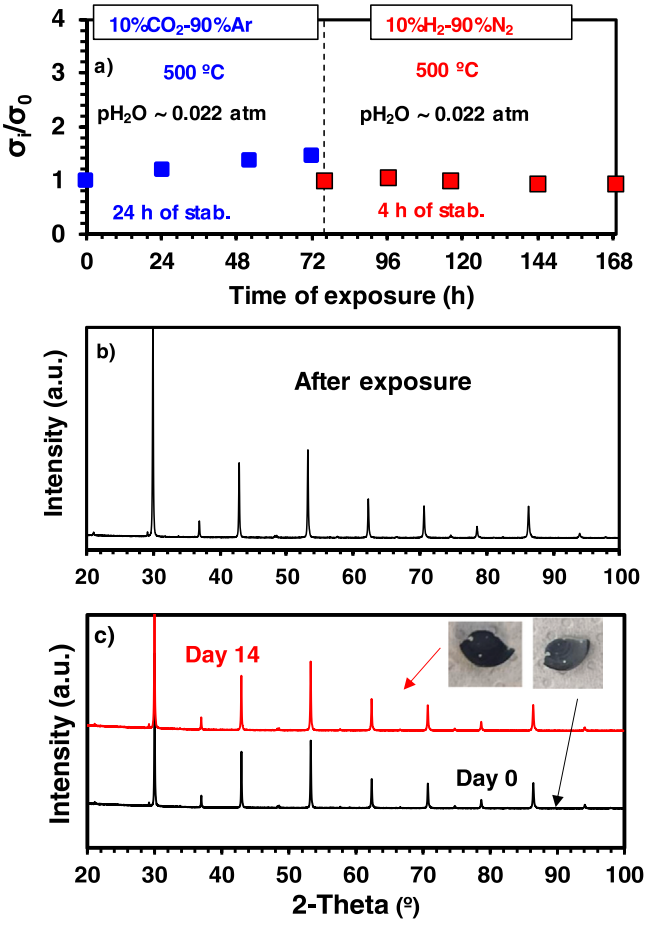

Fig. 6. a) Fraction of initial conductivity as a function of exposure time for sol-gel prepared BZY20-10F with Ba excess and 4 mol% ZnO sintered at 1200 °C exposed to atmospheres of wet 10 % CO_2:90 % Ar then 10 % H_2:90 % N_2; b) XRD pattern of sample after stability tests in different wet atmospheres; c) XRD patterns of BZY20-10F before and after exposure to laboratory air for 14 days; corresponding photographic images of pellet fracture are shown as insets.

3.4. Electrical properties

Impedance spectra of the F-doped BZY20 were collected in atmospheres of wet and dry O_2 and N_2 (similar data for the F-free analogue prepared in the same way have been published recently [18]). Selected low-temperature data, where grain and grain-boundary processes may be resolved, are shown in Fig. 7. The spectra were fitted with an equivalent circuit consisting of a serial association of simple parallel RQ elements for each process (continuous black lines, Fig. 7). The insets at 150 °C (Fig. 7a) and d)) show a magnified region close to the origin, where responses with capacitance values in the range 10^{-11}-10^{-12} F·cm^{-1}, typical of the grain-interior (bulk) process, are observed [33]. As temperature increases (≥ 250 °C), the arc in the high-frequency region is no longer observable since the bulk resistance decreases and the associated relaxation frequency is beyond the instrumental detection limit (insets of Fig. 7b), c), e) and f)).

The BZY20-10F sample exhibits a similar response in the mid-low frequency range as that observed for both BZY20, prepared in the same manner [18], and other zirconate-based perovskites [54,55], in which two processes with capacitances in the order of 10^{-10}-10^{-9} F·cm^{-1} may be discerned. As reported previously [56], different interpretations of the arc at lower frequencies may be responsible for the broad range of reported conductivity values for the BZY system. Several authors remark that the two superimposed semicircles are associated with the grain-boundary contributions [54,55], and may arise from the segregation of amorphous secondary phases leading to inhomogeneities, which may cause a distribution of different grain-boundary conductivities [57]. In the present case, according to the Raman results, which do not provide evidence of secondary phases with F, it appears that fluorine is, at least partially, located in the perovskite lattice, substituting the host oxygen. However, in addition to F, amorphous second phases may also arise from the excess Ba content of the starting composition and the ZnO sintering aid, which may be present both in the grains and grain boundaries [17].

The bulk response of the spectra collected at low temperature in wet N_2 (Fig. 7a), b) c)) shifts to lower resistance with respect to the values exhibited in dry O_2 (Fig. 7d), e) and f)). These results are the consequence of different species dominating the electrical transport at each atmosphere in the low-temperature region, protons in wet N_2 and oxide ions in dry O_2, as will be clarified below.

A comparison of the dependence of the total conductivity of BZY20-10F as a function of temperature in dry oxygen and nitrogen atmospheres is shown in Fig. 8a). Conductivity in the high-temperature range is greater in dry O_2 than in dry N_2 due to the higher contribution of electronic species, since the concentration of electron holes in O_2 increases at elevated temperatures in comparison to the more reducing N_2 atmosphere according the defect reaction:

$$V_O^{\cdot\cdot} + 1/2O_2 \leftrightarrow O_O^{\times} + 2h^{\cdot} \quad (4)$$

As temperature in the dry conditions decreases, the conductivities in O_2 and N_2 tend to converge, indicating a lower contribution to transport of electronic species. This arises from the annihilation of electron holes and the predominance of oxygen vacancies at low temperature due to the endothermic character of Eq. 4 [22]. A greater conductivity is registered in humidified N_2 in comparison to dry N_2 below ~ 550 °C, Fig. 8b), suggesting that protonic species are the principal charge carriers in this temperature regime in humid atmospheres. Whereas total conductivity practically doubles in wet N_2 compared to dry N_2 at 500 °C (3.9×10^{-4} and 2×10^{-4} S.cm^{-1}, respectively), it is almost four times greater in wet compared to dry N_2 atmospheres at 300 °C (9.2×10^{-6} and 2.5×10^{-6} S cm^{-1}, respectively), revealing the major role of protons in

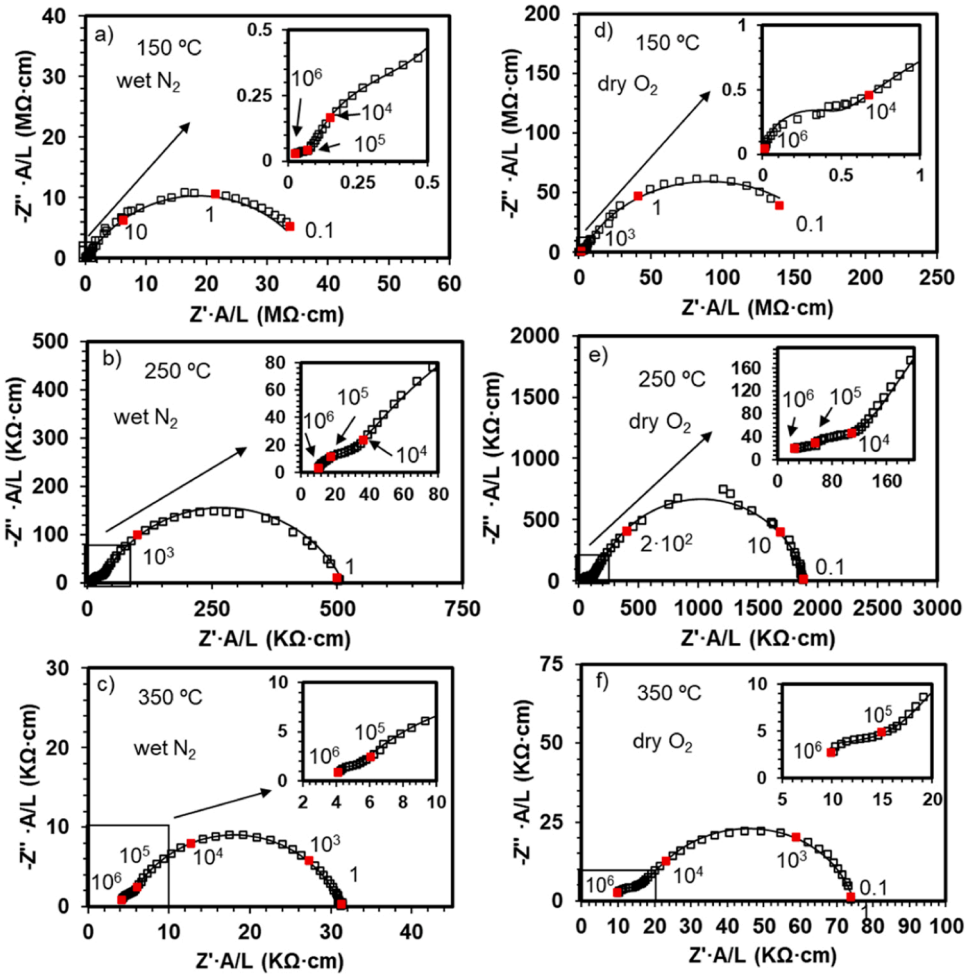

Fig. 7. Impedance spectra for BZY20-10F densified at 1200 °C obtained under (a, b, c) wet N_2 and (d, e, f) dry O_2 at (a, d) 150 °C, (b, e) 250 °C and (c, f) 350 °C. Continuous lines correspond to fitting results employing equivalent-circuit analysis. Insets in the figures correspond to magnifications in the high-frequency range. Selected reference frequencies are indicated.

electrical transport in wet conditions as temperature decreases. The protonic-defect concentration decreases as temperature increases as a result of the exothermic nature of the hydration reaction [21]:

$$V_O^{\cdot\cdot} + O_O^x + H_2O \leftrightarrow 2OH_O^{\cdot} \quad (5)$$

Fig. 8c)-f) show the conductivities of grain and grain boundary under dry and wet conditions for both oxygen and nitrogen atmospheres. Electrical transport is dominated by the grain-boundary process in the low-mid temperature regime; however, as temperature rises, the bulk conductivity seems to be the dominating process, with values close to total conductivity for temperatures higher than ~ 500 °C. The apparent change in slope is likely attributable to the change in dominating charge carriers from ions to electron holes with increasing temperature. The total conductivity is ~ 1.2×10^{-3} S·cm^{-1} at 600 °C in wet N_2, Fig. 8f), which is similar to values reported in the literature for the parent barium-zirconate compositions in wet reducing conditions [16,18,58–61], although some discrepant higher conductivities have also been reported [56,62]. The variance between literature reports may be, in part, associated to the interpretation of the low-frequency response of the impedance spectra, which is differently ascribed to the grain boundary or the electrode processes [55]. Moreover, the existence of two different cubic perovskite polymorphs, with conductivities ranging between 10^{-3} and 10^{-2} S·cm^{-1}, as was reported for $BaZr_{0.9}Y_{0.1}O_{3-\delta}$ [63], may also result in discrepancies.

Fig. 9a) and b) compare the total, bulk and grain-boundary conductivities of BZY20 and BZY20-10F. In general, it can be stated that the conductivity data for the F-doped sample lie in a similar range to those of its F-free analogues, and no firm conclusions about the role of F on the electrical transport properties of BZY can be drawn. We also note that the reported conductivity values for BZY are notorious for exhibiting a wide range of values in comparable conditions, which may result from different microstructures, compositional inhomogeneities and differing interpretation of impedance data, as alluded to earlier.

On consideration of the concentration of ionic charge-carriers alone, we should expect a lower oxide-ion conductivity (dry conditions) or proton conductivity (wet conditions) for the F-doped analogue (Eqs. (2) and (3)). Accordingly, Zhou et al.[23] obtained lower conductivities for F- and Cl- doped $BaCe_{0.9}Gd_{0.1}O_{3-\delta}$, which was directly associated to the expected decrease of oxygen-vacancy concentration on halogen doping. Nevertheless, Gao et al. [19] reported improved conductivity of BZY20-10F in comparison to the undoped material. Belova et al. [64] also documented enhanced conductivity as fluorine dopant content increases in the proton conductor $Ba_4Ca_2Nb_2O_{11}$, and suggested that the more ionic M-F bonds compared to M-O make the M-O bonds more covalent with the consequence that the proton in a fragment F-M-O becomes more acidic and mobility of the proton increases. It was also argued that Cl- and F-doping of the double perovskite $Ba_2CaNbO_{6-\delta}$ increases oxide-ion and proton mobilities due to repulsion between the donor $Cl_O^{\bullet}$ or $F_O^{\bullet}$ dopants and the positive mobile species (oxide-ion vacancies ($V_O^{\bullet\bullet}$) or protons ($OH_O^{\bullet}$) [20]. It is likely that halogen dopant content is critical to determining if there are determinable differences between halogen-containing and halogen-free compositions, and, if so,

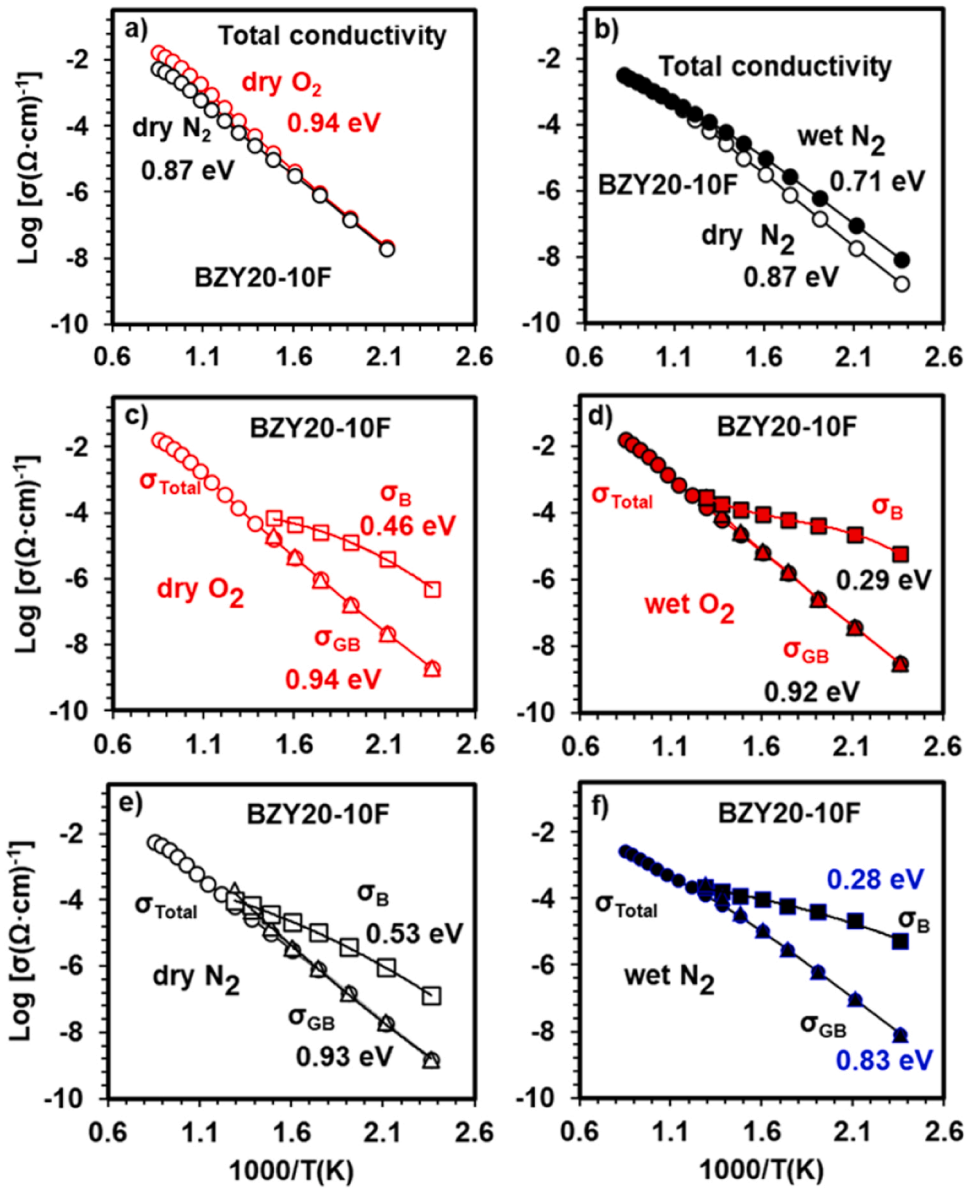

Fig. 8. Temperature dependence of total conductivity of BZY20–10F under a) dry nitrogen and b) wet nitrogen; grain, grain boundary and total conductivities under c) dry oxygen, d) wet oxygen, e) dry nitrogen and f) wet nitrogen.

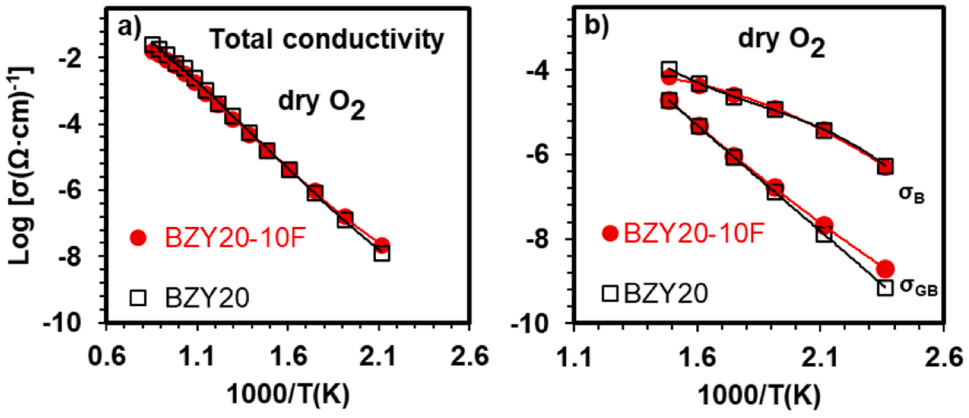

Fig. 9. Comparison of a) total conductivity and b) grain and grain-boundary conductivities as a function of temperature for BZY20–10F (closed circles) and BZY20 (open squares) under dry oxygen.

whether enhanced mobility or lower charge-carrier concentration is the most dominating factor. In the present study, the similar electrical behaviour between BZY20-10F and BZY20 appears to indicate a negligible effect of fluorine doping on the oxide-ion vacancy content or ion mobility, resulting in a similar conductivity to BZY. As both the bulk and grain-boundary processes are also similar, this suggests that any possible F-based segregation does not significantly alter the space-charge grain-boundary properties. It is worth recalling that evaporation of halogens, for example in the case of Br-doped $BaCe_{0.9}Y_{0.1}O_{3-\delta}$, can affect the electrical properties by changing the stoichiometry of the material [21], which complicates the comparison of systems with different compositions prepared with different high temperature ranges, where the halogen content may not be controlled. Nevertheless, in the present study, the presence of F in the sintered body densified at low temperature has been demonstrated with different spectroscopic techniques.

4. Conclusions

Low-temperature synthesis and densification of BZY doped with fluorine was achieved employing a sol-gel route with alkoxide precursors. The formation of reactive nanopowders with Ba excess in the starting composition and the addition of ZnO sintering aid contributes to a low sintering temperature of 1200 °C, necessary for high densification with limited halogen loss. The presence of flourine in materials sintered at this temperature was confirmed by Raman spectroscopy and ToF-SIMS. X-ray photoelectron and Raman spectroscopies indicate that the presence of F inhibits surface carbonate formation, suggesting improved long-term stability for the F-doped phase. Conductivity studies in both wet CO_2- and H_2-containing atmospheres over prolonged periods at 500 °C demonstrated good stability of F-containing BZY. Electrical measurements indicated that the F-doped samples exhibit conductivity values within the expected range for BZY-based ceramics.

Declaration of Competing Interest

The authors declare that they have no known competing financial interests or personal relationships that could have appeared to influence the work reported in this paper.

Acknowledgements

We thank MICINN in Spain for the concession of projects RTI2018–095088-B-I00, RTI2018–095373-J-I00 and predoctoral grant BES-2016–077023. The technical and other support provided by Daniel Gamarra (Facility of Analysis and Characterization of Solids and Surfaces of SAIUEx, financed by UEX, Junta de Extremadura, MICINN, FEDER and FSE) is recognised.

Appendix A. Supporting information

Supplementary data associated with this article can be found in the online version at doi:10.1016/j.jeurceramsoc.2022.09.042.

References

[1] H.G. Bohn, T. Schober, Electrical Conductivity of the High-Temperature Proton Conductor $BaZr_{0.9}Zr_{0.1}O_{2.95}$, J. American Ceram. Soc 83 (2000) 768–772.
[2] K.D. Kreuer, Proton -Conducting Oxides, Annu. Rev. Mater. Res. 33 (2003) 333–359, https://doi.org/10.1146/annurev.matsci.33.022802.091825.
[3] C. Duan, R.J. Kee, H. Zhu, C. Karakaya, Y. Chen, S. Ricote, A. Jarry, E.J. Crumlin, D. Hook, R. Braun, N.P. Sullivan, R. O'Hayre, Highly durable, coking and sulfur tolerant, fuel-flexible protonic ceramic fuel cells, Nature 557 (2018), https://doi.org/10.1038/s41586-018-0082-6.
[4] S. Fang, S. Wang, K.S. Brinkman, F. Chen, A sinteractive Ni-$BaZr_{0.8}Y_{0.2}O_{3-\delta}$ composite membrane for hydrogen separation, J. Mater. Chem. A 2 (2014) 5825–5833, https://doi.org/10.1039/c3ta14777k.
[5] W.A. Rosensteel, N.P. Sullivan, Fabrication and hydrogen permeation through novel $BaZr_{0.9}Y_{0.1}O_{3-\Delta}$ – Cu composite ceramic-metallic membranes, Int. J. Hydrogen Energy 42 (2017) 4216–4223, https://doi.org/10.1016/j.ijhydene.2016.10.048.
[6] S.H. Morejudo, R. Zanon, S. Escolastico, I. Yuste-Tirados, H. Malerod-Fjeld, P. K. Vestre, W.G. Coors, A. Martinez, T. Norby, J.M. Serra, C. Kjolseth, Direct conversion of methane to aromatics in a catalytic co-ionic membrane reactor, Science 353 (2016) 563–566, https://doi.org/10.1126/science.aag0274.
[7] X. Chi, Z. Wen, J. Zhang, Y. Liu, A novel facile way to synthesize proton-conducting $Ba(Ce,Zr,Y)O_3$ solid solution with improved sinterability and electrical performance, J. Eur. Ceram. Soc. 35 (2015) 2109–2117, https://doi.org/10.1016/j.jeurceramsoc.2015.01.012.
[8] T.L. Simonenko, M.V. Kalinina, N.P. Simonenko, E.P. Simonenko, O.V. Glumov, N. A. Mel'nikova, I.V. Murin, O.O. Shichalin, E.K. Papynov, O.A. Shilova, V. G. Sevastyanov, N.T. Kuznetsov, Synthesis of $BaCe_{0.9-x}Zr_xY_{0.1}O_{3-\Delta}$ nanopowders and the study of proton conductors fabricated on their basis by low-temperature spark plasma sintering, Int. J. Hydrogen Energy. 44 (2019) 20345–20354, https://doi.org/10.1016/j.ijhydene.2019.05.231.
[9] N. Ito, H. Matsumoto, Y. Kawasaki, S. Okada, T. Ishihara, Introduction of In or Ga as second dopant to $BaZr_{0.9}Y_{0.1}O_{3-\delta}$ to achieve better sinterability, Solid State Ionics. 179 (2008) 324–329, https://doi.org/10.1016/j.ssi.2008.02.047.
[10] P. Babilo, S.M. Haile, Enhanced Sintering of Yttrium-Doped Barium Zirconate by Addition of ZnO, J. Amercian Ceram. Soc. 2368 (2005) 2362–2368, https://doi.org/10.1111/j.1551-2916.2005.00449.x.
[11] S. Tao, J.T.S. Irvine, A stable, easily sintered proton-conducting oxide electrolyte for moderate-temperature fuel cells and electrolyzers, Adv. Mater. 18 (2006) 1581–1584, https://doi.org/10.1002/adma.200502098.
[12] S. Ricote, N. Bonanos, Enhanced sintering and conductivity study of cobalt or nickel doped solid solution of barium cerate and zirconate, Solid State Ionics 181 (2010) 694–700, https://doi.org/10.1016/j.ssi.2010.04.007.
[13] J.-S. Park, J.-H. Lee, H.-W. Lee, B.-K. Kim, Low temperature sintering of $BaZrO_3$-based proton conductors for intermediate temperature solid oxide fuel cells, Solid State Ionics 181 (2010) 163–167, https://doi.org/10.1016/j.ssi.2009.06.015.
[14] Y. Yamazaki, R. Hernandez-Sanchez, S.M. Haile, High total proton conductivity in large-grained yttrium-doped barium zirconate, Chem. Mater. 21 (2009) 2755–2762, https://doi.org/10.1021/cm900208w.
[15] J. Tong, D. Clark, L. Bernau, M. Sanders, R. O'Hayre, Solid-state reactive sintering mechanism for large-grained yttrium-doped barium zirconate proton conducting ceramics, J. Mater. Chem. 20 (2010) 6333–6341, https://doi.org/10.1039/c0jm00381f.
[16] S. Tao, J.T.S. Irvine, Conductivity studies of dense yttrium-doped $BaZrO_3$ sintered at 1325 °C, J. Solid State Chem. 180 (2007) 3493–3503, https://doi.org/10.1016/j.jssc.2007.09.027.
[17] H.S. Soares, I. Antunes, F.J.A. Loureiro, D. Pérez-Coll, M.G. Willinger, A. D. Brandão, G.C. Mather, D.P. Fagg, Effect of the addition mechanism of ZnO sintering aid on densification, microstructure and electrical properties of $Ba(Zr,Y)O_{3-\delta}$ proton-conducting perovskite, Int. J. Hydrogen Energy 46 (2021) 26466–26477, https://doi.org/10.1016/j.ijhydene.2021.05.109.
[18] Á. Triviño-Peláez, D. Pérez-Coll, M. Aparicio, D.P. Fagg, J. Mosa, G.C. Mather, D. Pérez Coll, M. Aparicio, D.P. Fagg, J. Mosa, G.C. Mather, Processing and characterisation of $BaZr_{0.8}Y_{0.2}O_{3-\delta}$ proton conductor densified at 1200 °C, J. Mater. Chem. A. 10 (2022) 4428–4439, https://doi.org/10.1039/d1ta09998a.
[19] J. Gao, Y. Liu, Y. Meng, M. Hu, K.S. Brinkman, Fluoride-Based Anion Doping: A New Strategy for Improving the Performance of Protonic Ceramic Conductors of the Form $BaZrO_3$, ChemElectroChem 7 (2020) 2242–2247, https://doi.org/10.1002/celc.202000154.
[20] N. Tarasova, I. Animitsa, Anionic doping (F^-, Cl^-) as the method for improving transport properties of proton-conducting perovskites based on $Ba_2CaNbO_{5.5}$, Solid State Ionics 317 (2018) 21–25, https://doi.org/10.1016/j.ssi.2018.01.001.
[21] Á. Triviño-Peláez, D. Pérez-Coll, G.C. Mather, Electrical properties of proton-conducting $BaCe_{0.8}Y_{0.2}O_{3-\delta}$ and the effects of bromine addition, Acta Mater. 167 (2019) 12–22, https://doi.org/10.1016/j.actamat.2019.01.028.
[22] Á. Triviño-Peláez, D. Pérez-Coll, J. Mosa, C. Ritter, U. Amador, G.C. Mather, Enhanced proton conductivity and stability of Ba-deficient $BaCe_{0.8}Y_{0.2}O_{3-\delta}$, J. Power Sources. 493 (2021) 3229691, https://doi.org/10.1016/j.jpowsour.2021.229691.
[23] H. Zhou, L. Dai, L. Jia, J. Zhu, Y. Li, L. Wang, Effect of fluorine, chlorine and bromine doping on the properties of gadolinium doped barium cerate electrolytes, Int. J. Hydrogen Energy. 40 (2015) 8980–8988, https://doi.org/10.1016/j.ijhydene.2015.05.040.
[24] A. Slodczyk, O. Zaafrani, M.D. Sharp, J. a Kilner, B. Dabrowski, O. Lacroix, P. Colomban, Testing the Chemical/Structural Stability of Proton Conducting Perovskite Ceramic Membranes by in Situ/ex Situ Autoclave Raman Microscopy, Membranes (Basel) 3 (2013) 311–330, https://doi.org/10.3390/membranes3040311.
[25] J.M. Polfus, B. Yildiz, H.L. Tuller, R. Bredesen, Adsorption of CO_2 and Facile Carbonate Formation on $BaZrO_3$, Surfaces, J. Phys. Chem. C. 122 (2018) 307–314, https://doi.org/10.1021/acs.jpcc.7b08223.
[26] R. Sažinas, M.F. Sunding, A. Thøgersen, I. Sakaguchi, T. Norby, T. Grande, J. M. Polfus, Surface reactivity and cation non-stoichiometry in $BaZr_{1-x}Y_xO_{3-\delta}$ (x = 0-0.2) exposed to CO_2 at elevated temperature, J. Mater. Chem. A. 7 (2019) 3848–3856, https://doi.org/10.1039/c8ta11021b.
[27] Y. Wang, H. Wang, T. Liu, F. Chen, C. Xia, Improving the chemical stability of $BaCe_{0.8}Sm_{0.2}O_{3-\delta}$ electrolyte by Cl doping for proton-conducting solid oxide fuel cell, Electrochem. Commun. 28 (2013) 87–90, https://doi.org/10.1016/j.elecom.2012.12.012.
[28] D. Pérez-Coll, G. Heras-Juaristi, D.P. Fagg, G.C. Mather, Transport-number determination of a protonic ceramic electrolyte membrane via electrode-

polarisation correction with the Gorelov method, J. Power Sources. 245 (2014) 445–455, https://doi.org/10.1016/j.jpowsour.2013.06.155.
[29] G. Heras-Juaristi, D. Pérez-Coll, G.C. Mather, Temperature dependence of partial conductivities of the $BaZr_{0.7}Ce_{0.2}Y_{0.1}O_{3-\delta}$ proton conductor, J. Power Sources. 364 (2017) 52–60, https://doi.org/10.1016/j.jpowsour.2017.08.011.
[30] Á. Triviño-Peláez, G.C. Mather, D. Pérez-Coll, M. Aparicio, J. Mosa, $SrZr_{0.9}Y_{0.1}O_{3-\delta}$ thin films by in-situ synthesis of triple alkoxide for protonic ceramic electrolyser membranes, J. Sol-Gel Sci. Technol. 95 (2020) 661–669, https://doi.org/10.1007/s10971-020-05338-4.
[31] G. Gorni, M.J. Pascual, A. Caballero, J.J. Velázquez, J. Mosa, Y. Castro, A. Durán, Crystallization mechanism in sol-gel oxyfluoride glass-ceramics, J. Non. Cryst. Solids. 501 (2018) 145–152, https://doi.org/10.1016/j.jnoncrysol.2018.01.031.
[32] J. Rodriguez-Carvajal, Recent advances in magnetic structure determination by neutron powder diffraction, Phys. B 192 (1993) 55–69.
[33] J.T.S. Irvine, D.C. Sinclair, A.R. West, Electroceramics: Characterisation by impedance spectroscopy, Adv. Mater. 2 (1990) 132–138.
[34] A. Magrez, T. Schober, Preparation, sintering, and water incorporation of proton conducting $Ba_{0.99}Zr_{0.8}Y_{0.2}O_{3-\delta}$: Comparison between three different synthesis techniques, Solid State Ionics. 175 (2004) 585–588, https://doi.org/10.1016/j.ssi.2004.03.045.
[35] R.D. Shannon, Revised effective ionic radii and systematic studies of interatomic distances in halides and chalcogenides, Acta Crystallogr. Sect. A. 32 (1976) 751–767, https://doi.org/10.1107/S0567739476001551.
[36] D. Marrocchelli, S.R. Bishop, H.L. Tuller, B. Yildiz, Understanding chemical expansion in non-stoichiometric oxides: Ceria and zirconia case studies, Adv. Funct. Mater. 22 (2012) 1958–1965, https://doi.org/10.1002/adfm.201102648.
[37] P. Seeharaj, T. Charoonsuk, P. Pasupong, P. Kim-Lohsoontorn, N. Vittayakorn, Phase formation, microstructure, and densification of yttrium-doped barium zirconate prepared by the sonochemical method, Int. J. Appl. Ceram. Technol. 13 (2016) 200–208, https://doi.org/10.1111/ijac.12436.
[38] P.S. Dobal, A. Dixit, R.S. Katiyar, Z. Yu, R. Guo, A.S. Bhalla, Phase transition behavior of $BaZr_xTi_{1-x}O_3$ ceramics, J. Raman Spectrosc. 32 (2001) 69–71, https://doi.org/10.1107/s0108767302094965.
[39] L.R. MacArio, M.L. Moreira, J. Andrés, E. Longo, An efficient microwave-assisted hydrothermal synthesis of $BaZrO_3$ microcrystals: Growth mechanism and photoluminescence emissions, CrystEngComm 12 (2010) 3612–3619, https://doi.org/10.1039/c004034g.
[40] P. Pasierb, S. Komornicki, M. Rokita, M. Rękas, Structural properties of Li_2CO_3-$BaCO_3$ system derived from IR and Raman, spectroscopy, J. Mol. Struct. 596 (2001) 151–156, https://doi.org/10.1016/S0022-2860(01)00703-7.
[41] M.M. Welander, D.J. Goettlich, T.J. Henning, R.A. Walker, Yttria-stabilized barium zirconate surface reactivity at elevated temperatures, MRS Commun. 10 (2020) 455–460, https://doi.org/10.1557/mrc.2020.43.
[42] C.S. Tu, R.R. Chien, V.H. Schmidt, S.C. Lee, C.C. Huang, Temperature-dependent structures of proton-conducting $Ba(Zr_{0.8x}Ce_xY_{0.2})O_{2.9}$ ceramics by Raman scattering and x-ray diffraction, J. Phys. Condens. Matter 24 (2012), https://doi.org/10.1088/0953-8984/24/15/155403.
[43] K.S. Blinn, Investigation of electrode surfaces in solid oxide fuel cells using Raman mapping and enhanced spectroscopy techniques, PhD thesis, Georgia Institute of Technology, 2012.
[44] R.L. McCreery, Raman Spectrscopy for Chemical Analysis, John Wiley & Sons, New York, 2000. ISBN: 978-0-471-25287-0.
[45] A. Slodczyk, P. Colomban, S. Willemin, O. Lacroix, B. Sala, Indirect Raman identification of the proton insertion in the high-temperature [Ba/Sr][Zr/Ti]O_3-modified perovskite protonic conductors, J. Raman Spectrosc. 40 (2009) 513–521, https://doi.org/10.1002/jrs.2157.
[46] S. Ruan, D.P. McMeekin, R. Fan, N.A.S. Webster, H. Ebendorff-Heidepriem, Y. B. Cheng, J. Lu, Y. Ruan, C.R. McNeill, Raman Spectroscopy of Formamidinium-Based Lead Halide Perovskite Single Crystals, J. Phys. Chem. C. 124 (2020) 2265–2272, https://doi.org/10.1021/acs.jpcc.9b08917.
[47] R.G. Niemann, A.G. Kontos, D. Palles, E.I. Kamitsos, A. Kaltzoglou, F. Brivio, P. Falaras, P.J. Cameron, Halogen Effects on Ordering and Bonding of $CH_3NH_3^+$ in $CH_3NH_3PbX_3$ (X = Cl, Br, I) Hybrid Perovskites: A Vibrational Spectroscopic Study, J. Phys. Chem. C. 120 (2016) 2509–2519, https://doi.org/10.1021/acs.jpcc.5b11256.
[48] R.B. Borade, A. Clearfield, Effect of fluoride ions on the acidic and catalytic properties of beta zeolite, J. Chem. Soc. Faraday Trans. 91 (1995) 539–547, https://doi.org/10.1039/FT9959100539.
[49] M.D. González, Y. Cesteros, P. Salagre, Establishing the role of Brønsted acidity and porosity for the catalytic etherification of glycerol with tert-butanol by modifying zeolites, Appl. Catal. A Gen. 450 (2013) 178–188, https://doi.org/10.1016/j.apcata.2012.10.028.
[50] L. Yu, S. Huang, S. Miao, F. Chen, S. Zhang, Z. Liu, S. Xie, L. Xu, A facile top-down protocol for postsynthesis modification of hierarchical aluminum-rich MFI zeolites, Chem. - A Eur. J. 21 (2015) 1048–1054, https://doi.org/10.1002/chem.201404817.
[51] P.J. Schmitz, Characterization of the Surface of $BaCO_3$ Powder by XPS, Surf. Sci. Spectra 8 (2001) 190–194, https://doi.org/10.1116/11.20011102.
[52] M.C. Blanco López, B. Rand, F.L. Riley, Identification of barium carbonate in barium titanate powders, Key Eng. Mater. 132–136 (1997) 252–255, https://doi.org/10.4028/www.scientific.net/kem.132-136.252.
[53] E. Desimoni, G.I. Casella, A.M. Salvi, T.R.I. Cataldi, A. Morone, XPS investigation of ultra-high-vacuum storage effects on carbon fibre surfaces, Carbon 30 (1992) 527–531, https://doi.org/10.1016/0008-6223(92)90171-R.
[54] A. Magrasó, C. Kjølseth, R. Haugsrud, T. Norby, Influence of Pr substitution on defects, transport, and grain boundary properties of acceptor-doped $BaZrO_3$, Int. J. Hydrogen Energy. 37 (2012) 7962–7969, https://doi.org/10.1016/j.ijhydene.2011.10.067.
[55] C. Kjølseth, H. Fjeld, Ø. Prytz, P.I. Dahl, C. Estournès, R. Haugsrud, T. Norby, Space–charge theory applied to the grain boundary impedance of proton conducting $BaZr_{0.9}Y_{0.1}O_{3-\delta}$, Solid State Ionics 181 (2010) 268–275, https://doi.org/10.1016/j.ssi.2010.01.014.
[56] P. Babilo, T. Uda, S.M. Haile, Processing of yttrium-doped barium zirconate for high proton conductivity, J. Mater. Res. 22 (2007) 1322–1330, https://doi.org/10.1557/jmr.2007.0163.
[57] J. Fleig, Influence of non-ideal microstructures on the analysis of grain boundary impedances, Solid State Ionics 131 (2000) 117–127, https://doi.org/10.1016/S0167-2738(00)00627-5.
[58] S. Ricote, L. Krishna, W.G. Coors, J.R. O'Brien, Conductivity behavior of $BaZr_{0.9}Dy_{0.1}O_{3-\delta}$, Solid State Ionics 314 (2018) 25–29, https://doi.org/10.1016/j.ssi.2017.11.010.
[59] S. Ricote, N. Bonanos, A. Manerbino, N.P. Sullivan, W.G. Coors, Effects of the fabrication process on the grain-boundary resistance in $BaZr_{0.9}Y_{0.1}O_{3-\delta}$, J. Mater. Chem. A. 2 (2014) 16107–16115, https://doi.org/10.1039/c4ta02848a.
[60] R.B. Cervera, Y. Oyama, S. Miyoshi, K. Kobayashi, T. Yagi, S. Yamaguchi, Structural study and proton transport of bulk nanograined Y-doped $BaZrO_3$ oxide protonics materials, Solid State Ionics 179 (2008) 236–242, https://doi.org/10.1016/j.ssi.2008.01.082.
[61] H.W. Kim, J. Seo, J.H. Yu, K.S. Yun, J.H. Joo, J. Moon, H.J. Park, Effect of cerium on yttrium-doped barium zirconate with a ZnO sintering aid: Grain and grain boundary protonic conduction, Ceram. Int. (2021), https://doi.org/10.1016/j.ceramint.2021.08.168.
[62] D. Han, K. Toyoura, T. Uda, Protonated $BaZr_{0.8}Y_{0.2}O_{3-\delta}$: Impact of Hydration on Electrochemical Conductivity and Local Crystal Structure, ACS Appl. Energy Mater. 4 (2021) 1666–1676, https://doi.org/10.1021/acsaem.0c02832.
[63] A.K. Azad, C. Savaniu, S. Tao, S. Duval, P. Holtappels, R.M. Ibberson, J.T.S. Irvine, Structural origins of the differing grain conductivity values in $BaZr_{0.9}Y_{0.1}O_{2.95}$ and indication of novel approach to counter defect association, J. Mater. Chem. 18 (2008) 3414–3418, https://doi.org/10.1039/b806190d.
[64] K. Belova, S. Baskakova, C. Argirusis, I. Animitsa, The effect of F-doping on the conductivity of proton conductor $Ba_4Ca_2Nb_2O_{11}$, Electrochim. Acta 193 (2016) 63–71, https://doi.org/10.1016/j.electacta.2016.02.052.